HIGH POWER LASER
SCIENCE AND ENGINEERING

RESEARCH ARTICLE

976 nm continuous-wave laser damage of Er:CaF$_2$ crystals

Haiyang Wang [1,2,3], Mengxia Wang [2,3], Zhen Zhang [4], Yuanan Zhao [2,3,†], Dawei Li [2,3,†],
Kun Shuai [2,3], Hailong Qiu [1,†], Zhonghan Zhang [4], Liangbi Su [4], and Jianda Shao [2,3,5]

[1] *Tianjin Key Laboratory of Functional Crystal Materials, Institute of Functional Crystals, Tianjin University of Technology, Tianjin, China*

[2] *Center of Materials Science and Optoelectronics Engineering, University of Chinese Academy of Sciences, Beijing, China*

[3] *Laboratory of Thin Film Optics, Shanghai Institute of Optics and Fine Mechanics, Chinese Academy of Sciences, Shanghai, China*

[4] *Shanghai Institute of Ceramics, Chinese Academy of Sciences, Shanghai, China*

[5] *Hangzhou Institute for Advanced Study, University of Chinese Academy of Sciences, Hangzhou, China*

Abstract

Er:CaF$_2$ crystals are crucial gain media for producing 3 μm mid-infrared (MIR) lasers pumped by 976 nm continuous-wave (CW) lasers owing to their low phonon energy and high conversion efficiency. This study investigated the damage characteristics and mechanism of Er:CaF$_2$ crystals irradiated with a 976 nm CW laser. The laser-induced damage threshold of Er:CaF$_2$ crystals with different Er^{3+} doping levels was tested; the damage morphology consists of a series of regular 70° cracks related to the angle of the crystal slip system on the surface. A finite-element model was used to calculate the temperature and stress fields of the crystals. The results indicated that the damage can be attributed to surface tensile stresses caused by the temperature gradient, and crystals with higher doping concentrations were more susceptible to damage owing to stronger light absorption. These findings provide valuable insights into the development of high-power MIR lasers.

Keywords: continuous-wave laser-induced damage; Er:CaF$_2$; mid-infrared laser; thermal stress

1. Introduction

The mid-infrared (MIR) band lies within the water absorption region and encompasses pivotal atmospheric transmission windows and numerous distinct molecular fingerprint regions[1,2]. Therefore, MIR lasers have significant application value in many fields, such as space communication, environmental monitoring, opto-electronic countermeasures and material processing[3–6]. Solid-state lasers, compared to other MIR technologies, offer advantages in compactness, stability, efficiency and beam quality[7–10]. The

most convenient method of achieving approximately 3 μm laser emission is to pump erbium-doped gain materials using an approximately 976 nm laser diode (LD)[11–13]. The unique energy-level structure of Er^{3+} ions enables them to exhibit cooperative up-conversion and achieve lasing efficiency beyond the Stokes limit[14,15]. Therefore, Er lasers near 3 μm are considered to be important MIR laser sources, along with Tm/Ho lasers near 2 μm and Nd/Yb lasers near 1 μm[16].

CaF$_2$ is an ideal material for laser applications owing to its low phonon energy, high optical transparency, high thermal conductivity and low absorption loss. Er:CaF$_2$ solid-state lasers exhibit high conversion efficiencies at low doping concentrations. Moreover, their low phonon energy prevents the laser self-termination phenomenon, which occurs in lasers where Er-doped oxide-based materials are used[17]. Quimby and Miniscalco[18] proposed that continuous-wave (CW) laser operation can be achieved in certain Er-doped media with low phonon energy. In a recent report, Wang *et al.*[19] achieved a CW laser output at a wavelength of 2.8 μm using a low doping concentration of 0.3% (atomic fraction) Er:CaF$_2$ crystal, with a slope efficiency of 21.4% and a power

Correspondence to: M. Wang, Laboratory of Thin Film Optics, Shanghai Institute of Optics and Fine Mechanics (SIOM), Chinese Academy of Sciences (CAS), Shanghai 201800, China. Email: wmx@siom.ac.cn; Y. Zhao, Laboratory of Thin Film Optics, SIOM, CAS, Shanghai 201800, China. Email: yazhao@siom.ac.cn; H. Qiu, Tianjin Key Laboratory of Functional Crystal Materials, Institute of Functional Crystals, Tianjin University of Technology, Tianjin 300384, China. Email: qiu@tjut.edu.cn

† These authors contributed equally to this work.

1

of 143 mW. Liu *et al.*[20] prepared a mixed 4% (atomic fraction) Er:CaF$_2$-SrF$_2$ crystal and investigated its laser performance. In a compact linear cavity, the CW laser output power reached 712 mW, with a maximum slope efficiency of 41.4%. A 5.04 W CW laser at 2799 nm was obtained in a 2% (atomic fraction) Er:CaF$_2$ crystal with double end pumping by two 976 nm LDs[21].

Laser-induced damage in crystals is currently a bottleneck factor that limits further increases in MIR laser power based on Er:CaF$_2$. The thermal effects within the crystal will intensify significantly as the laser pump power increases. When the power reaches a threshold, the crystal could be damaged, resulting in the inability of the laser system to produce laser light[22–24].

In a previous study, the KrF excimer laser-induced damage characteristics of three crystal faces of CaF$_2$ crystals were investigated, and the mechanism of material removal was found to be closely related to the cleavage surface and sliding direction[25]. Research has been conducted on the interaction between the material and laser, as well as the transformation of CaF$_2$ under ultraviolet (UV) pulsed laser irradiation, resulting in the formation of nanoscale defects in the irradiated area. Studies have shown that this process induces fracturing of CaF$_2$ crystals and localized vitrification of the material[26–28]. Research in this area has primarily concentrated on pulsed laser damage in the UV range. However, there are no reports on the mechanisms of damage caused by high-power CW laser irradiation. It is essential to analyze the causes of crystal damage and explore the underlying mechanisms to enhance MIR laser output power.

Laser-induced damage processes with different pulse widths may involve multiphoton absorption, avalanche ionization, heat diffusion and deposition, plasma shock wave formation, material melting and mechanical fracturing[29–31]. For CW lasers, the thermal effects that cause an increase in material temperature and thermal stress dominate the damage process[32,33]. Under CW laser radiation, damage to optical components results primarily from the inherent absorption of the material and thermal deposition owing to absorption defects. This causes the temperature to increase, resulting in organic damage, such as melting, vaporization and crack formation, owing to thermal–mechanical coupling. It also induces changes in optical performance, thereby affecting the functionality of the component or the entire system. For gain crystals, high-power laser irradiation induces temperature gradients, which consequently trigger thermal stress, stress birefringence and thermal lensing effects, thereby affecting the optical performance, reducing the beam quality of the output laser and even causing damage to the laser medium[34]. Therefore, thermal effect analysis is of utmost importance for enhancing the laser-induced damage threshold (LIDT) of crystals, particularly when considering factors such as surface processing quality and ion doping concentration.

In this study, a CW laser damage test platform was constructed to investigate crystal damage under high-power 976 nm continuous laser irradiation. The laser damage thresholds of Er:CaF$_2$ crystals with different doping concentrations were determined using this system. Considering the effect of doping on the absorption and mechanical properties of the crystals[35], the key factors leading to the differences in the laser damage resistance of samples with different doping concentrations were found in conjunction with the test results. To investigate the damage mechanism of the crystals, we established a three-dimensional heat conduction and thermal stress model to determine the temperature and stress fields of the crystals during irradiation at different powers. The damage mechanism of the crystals under CW laser irradiation was analyzed from the perspective of thermal stresses. We confirmed that the main reason for the fracturing of the Er:CaF$_2$ crystals was that the circumferential stresses reached the tensile strength of the crystals. In addition, the effects of different Er doping concentrations on the LIDT were analyzed.

2. Sample and experimental methods

The $^4I_{13/2} \rightarrow {}^4I_{15/2}$ cascade jump at low doping concentration has a higher conversion efficiency compared to MIR lasers with high doping concentration and co-doping of Er^{3+} and Pr^{3+}. In order to achieve efficient MIR laser output, the damage mechanism of low-doped Er:CaF$_2$ was investigated.

Er:CaF$_2$ crystals with doping concentrations of 1% and 2% were successfully grown using the temperature-gradient method. The absorption spectroscopy is shown in Figure S1 in the Supplementary Material. The crystals were cut into blocks measuring 3 mm × 3 mm × 8 mm. The ends were polished without coating, and their spectral characteristics have been well-documented in previous studies[36].

The setup for the continuous-laser-damage threshold test is shown in Figure 1(a), through which laser loading, temperature control and recording and damage monitoring of the crystal were achieved. The pump source was an LD with a central wavelength of 976 nm (BWT, DS3-51512-K976AASRN). The maximum output power of the laser is 60 W (D_{core} = 105 μm, numerical aperture (NA) = 0.22). The beam profile was measured using an Ophir and Spiricon beam analyzer. The spatial distribution of the laser beam was approximated as a Gaussian distribution with a $1/e^2$ beam diameter of 160 μm at the focal point. A schematic of the CW laser damage test method is shown in Figure S2 in the Supplementary Material.

To eliminate threshold differences between samples of the same concentration owing to internal quality differences between batches of crystals or processing factors, we tested two pieces of each type of crystal. The damage thresholds of samples with different doping concentrations are shown
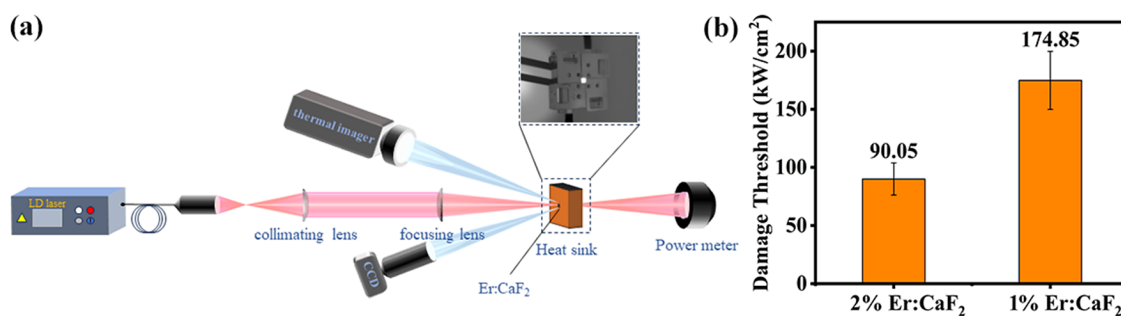
Figure 1. (a) Schematic of the experimental setup for a CW laser irradiation system. (b) Thresholds of Er:CaF$_2$ crystals with different doping concentrations under CW laser irradiation at 976 nm.

in Figure 1(b). The LIDTs of the 1% Er:CaF$_2$ crystals were 192.5 and 157.2 kW/cm^2. The LIDTs of the 2% Er:CaF$_2$ crystals were 99.8 and 80.3 kW/cm^2. Crystals with low doping concentrations have a higher damage threshold, which can be attributed to the distinct physical properties of crystals with different doping concentrations, such as thermal conductivity, coefficient of thermal expansion, absorption coefficient and fracture toughness[35,37]. After the experiment, the damage morphology was characterized using optical microscopy and scanning electron microscopy (SEM).

3. Damage morphology analysis

The CW laser-induced damage morphologies of 1% and 2% Er:CaF$_2$ are shown in Figure 2. The SEM images clearly show material cracking and splitting within the damaged areas. Figure 2(a) shows the damage morphology of the 1% Er:CaF$_2$ crystal, while Figure 2(c) shows an enlarged view of some of the damaged pits shown in Figure 2(a). The damage morphology exhibits a distinct 70° angle, which is exclusive to the (110) crystal plane of CaF$_2$ crystals. If damage occurs on the (111) and (100) planes, which are the other frequently used planes, the resulting cracks will exhibit angles of 60° and 90°, respectively. The CaF$_2$ crystal has a face-centered cubic structure, in which the slip system is {100} <110> and the cleavage plane is {111}. The angle of the regular cracks corresponds to the angle between the slip system at the crystal surface[28]. The SEM image shows a fully penetrating crack in the damaged region, with several massive fragments embedded in the crack. The core area of the severe fracture was surrounded by cracks oriented in a specific direction. Figure 2(b) shows the damage morphology of the 2% Er:CaF$_2$ crystal, and Figure 2(d) shows
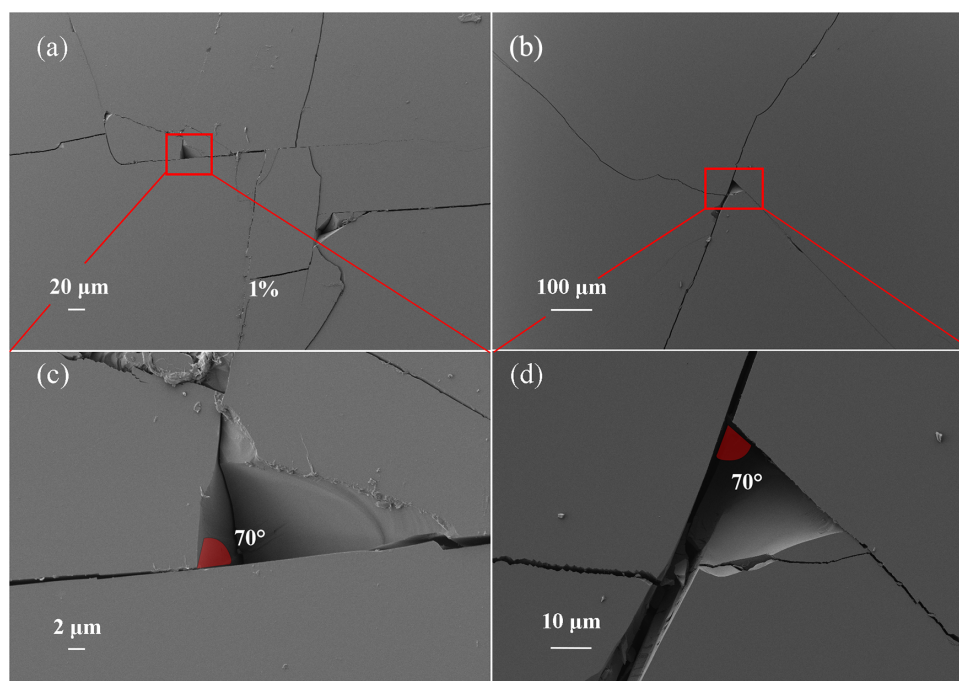
Figure 2. SEM images of typical damage morphology. (a) 1% Er:CaF$_2$ and (b) 2% Er:CaF$_2$ top views of the damage region resulting from CW laser irradiation, respectively. (c), (d) Magnified images of the rectangular region.

a magnified view of a part of the damaged region, again showing cracks at an angle of 70°, as well as multiple cracks that were more densely packed and parallel-oriented. No melting residue is observed in the damaged crater. The overall damage patterns were consistent for both crystals. Temperature gradients create thermal stresses that promote the creation or expansion of cracks in optical materials. This damage is related to microcracks and the thermal properties of the material, with the coefficient of thermal expansion being the most critical. The damage included cracks, bulk removal and splattered fragments in the vicinity of cracks. The damage is primarily characterized by a significant increase and expansion of cracks. Laser-driven crack formation and expansion, including long cracks and microcracks, divide the damaged areas into several regions. These sharp cracks and splitting patterns indicated that the material was subjected to significant mechanical stress under CW laser irradiation.

4. Theoretical calculation and discussion

The main mechanisms of CW laser-induced damage are vaporization and melting of the material due to elevated temperature and fracture of the material due to thermal stress; studying the temperature increase and stress in the crystal during laser irradiation can further elucidate the damage mechanism of Er:CaF$_2$. Finite-element numerical calculations are important for solving the thermal effects and thermal stresses. The temperature and stress tensors inside the crystal can be accurately determined by building correlation models and applying appropriate boundary conditions. Under the influence of the pump light, the spontaneous and excited radiation of doped ions, up-conversion and nonradiative relaxation between energy levels have negligible effects on the temperature field[38].

4.1. Thermodynamic modeling of crystals

To calculate the temperature and stress fields of Er:CaF$_2$ under 976 nm laser irradiation, based on heat transfer theory and solid mechanics, we developed a thermodynamically coupled physical model. A schematic of the physical model is shown in Figure S3 (Supplementary Material), which can be used to calculate the temperature and stress fields of a crystal at different times. The physical parameters of CaF$_2$ are listed in Table S1 (Supplementary Material).

4.2. Calculation of the temperature field of laser-pumped crystals

Under CW laser irradiation, crystals undergo temperature variations upon energy absorption. Through the principles of energy conservation and Fourier's heat conduction law,

the expression for the temperature at any position at time t can be obtained as follows:

$$\rho C_\mathrm{p} \frac{\partial T}{\partial t} + \rho C_\mathrm{p} \boldsymbol{u} \cdot \nabla T = Q_\mathrm{v} + k\nabla^2 T, \tag{1}$$

where T represents the temperature, k represents the thermal conductivity, C_p represents the constant pressure heat capacity, ρ represents the density, $\boldsymbol{u}$ represents the displacement and Q_v represents the thermal source function within the crystal, measured in units of W/m^3. When a Gaussian laser beam pumps the crystal, its thermal source function of the crystal is as follows:

$$Q(x,y,z) = (1-R)\frac{2P}{\pi w(z)^2}\exp\left(\frac{-2\left(x^2+y^2\right)}{w(z)^2}\right)\exp\left(-\alpha z\right)\frac{w_0^2}{w(z)^2}\alpha, \tag{2}$$

where $w(z)$ represents the Gaussian beam spot radius at distance z from the waist position:

$$w(z) = w_0\sqrt{1+\left(\frac{z}{z_\mathrm{R}}\right)^2}, \tag{3}$$

and $z_\mathrm{R} = \frac{\pi w_0^2}{M^2\lambda}$, where w_0 is the waist radius of the pump beam (the radius at which the energy is reduced to $1/e^2$ of the peak energy), R is the reflectance, α is the absorption coefficient of the crystal for the 976 nm pump beam, $\frac{\partial I}{\partial z} = \alpha(T)I$, λ is the wavelength of the pump laser and P is the pump power.

Under ideal conditions, the lateral sides of the crystal are maintained at a constant temperature by cooling water, whereas the end faces are cooled by air convection. This scenario is related to the concept of an ideal cooling mechanism. However, in most realistic and common scenarios, the crystal is cooled through air convection or an imperfect cooling system. In the cases, the boundary conditions are as follows:

$$k\frac{\partial T}{\partial l} = h_\mathrm{s}\left(T - T_0\right), \tag{4}$$

where h_s represents the heat transfer coefficient of various surfaces and T_0 denotes the ambient temperature in the surrounding natural environment.

The heat transfer coefficients were set to 25 and 820 W/(m^2·K) for the end and side surfaces, respectively, based on the experimental results of CW laser pumping of Er:CaF$_2$ crystals at different powers. The laser incidence angle was set to 0°. The relationship between the maximum temperature of the incident surface and the irradiation power was calculated for crystals with different doping concentrations.

The relationship between the maximum temperature of the sample end surface and pump power was recorded using a thermal imager (FLIR), and the results obtained were consistent with those obtained from numerical calculations,
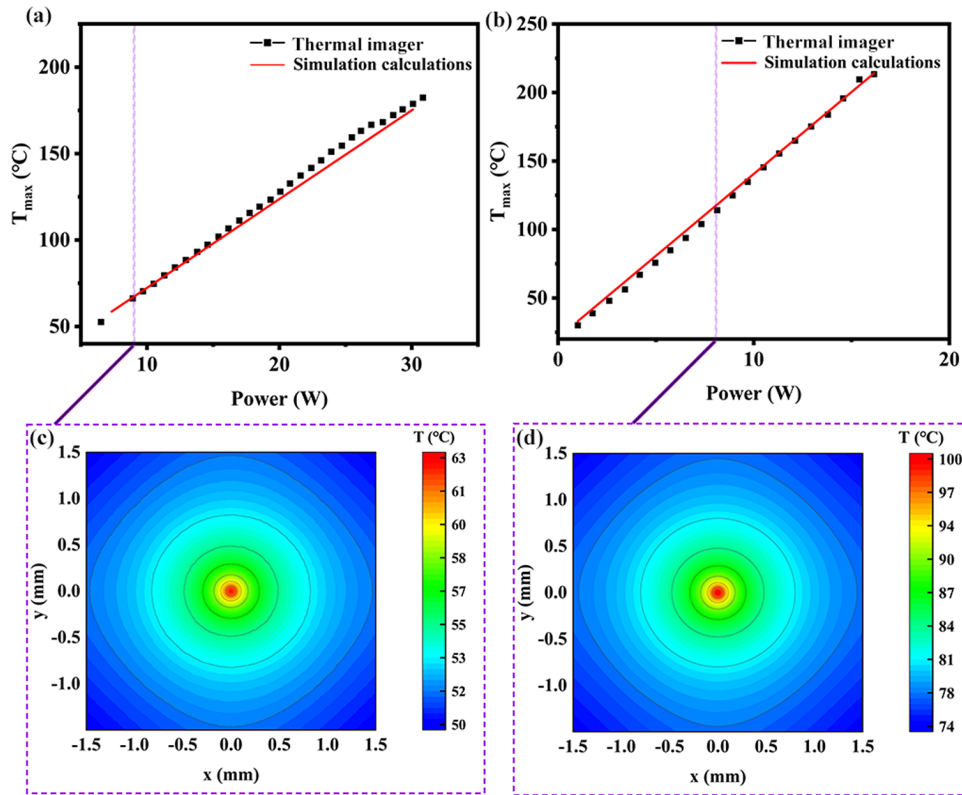
Figure 3. Relationship between the maximum temperature and pump power at the incidence surface of the (a) 1% Er:CaF$_2$ and (b) 2% Er:CaF$_2$. The temperature field at the incidence surface of (c) 1% Er:CaF$_2$ and (d) 2% Er:CaF$_2$, under a pump power of 8 W.

which verified the correctness of the theoretical model. Under CW laser irradiation, the maximum temperature of the crystal surface and pump power were linearly correlated, as shown in Figure 3.

The power versus maximum surface temperature for crystals with different doping concentrations is shown in Figure 3. The maximum temperature of the 1% Er:CaF$_2$ end surface increased from 53°C to 182°C when the incident power increased from 5 to 32 W (pump power when damage occurs in 1% Er:CaF$_2$). Similarly, the center temperature of the 2% Er:CaF$_2$ incident surface increased from 32°C to 218°C when the incident power increased from 2 to 17 W (pump power when damage occurs in 2% Er:CaF$_2$). The temperature increase of the crystals with higher doping concentrations was higher, which was caused by the higher absorption of light by the crystals with higher doping concentrations.

The temperature field on the incident surface of the Er:CaF$_2$ crystals with two different doping concentrations at a pump power of 8 W is shown in Figure 3. The temperature distribution patterns were similar, with the highest temperature occurring at the center of the incidence surface. The center temperatures of the 1% and 2% Er:CaF$_2$ crystals were 62°C and 97°C, respectively. The temperature decreased continuously as the distance from the center of the incident surface increased.

The damage of many media under laser irradiation is caused by the melting of the material at ultrahigh temperatures[39,40]. In this study, the temperatures (1% Er:CaF$_2$, 182°C; 2% Er:CaF$_2$, 218°C) at the surface of the crystals when damage occurred were significantly lower than their melting point (1362°C). The analysis of the crystal damage morphology revealed that stress was a key factor. Therefore, stress calculations were conducted.

### 4.3. Calculation of the stress field in laser-pumped crystals

To further investigate the damage mechanism of CaF$_2$, we must compute the stress state inside the crystal using the temperature field results. From a stress perspective, Newton's second law can be expressed as follows:

$$\nabla \cdot \sigma + f = \rho \frac{\partial^2 u}{\partial t^2}. \tag{5}$$

Based on the three-dimensional generalization of Hooke's law,

$$\sigma_{ij} = C\varepsilon_{ij}. \tag{6}$$

Here, $\varepsilon = \alpha(T - T_{\text{ref}})$ and C is the elastic stiffness matrix of the material. The optimal method for measuring
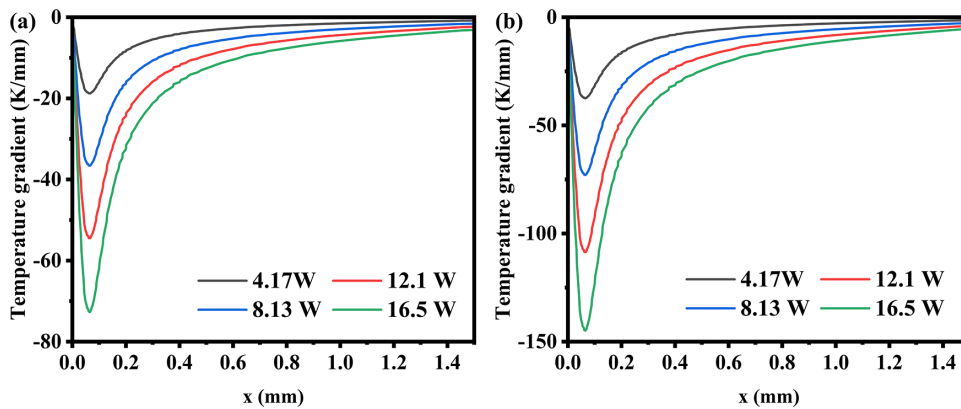
Figure 4. Temperature profiles in the x-axis direction of the incidence surface for 1% and 2% Er:CaF$_2$ for pump power from 4.17 to 16.50 W using a three-dimensional finite-element simulation model.

elastic constants involves the propagation of sound waves in solids[41]:

$$\sigma_x = \frac{E}{1+\nu}\left(\varepsilon_{xx} + \frac{\nu}{1-2\nu}\left(\varepsilon_{xx} + \varepsilon_{yy} + \varepsilon_{zz}\right)\right),$$

$$\sigma_y = \frac{E}{1+\nu}\left(\varepsilon_{yy} + \frac{\nu}{1-2\nu}\left(\varepsilon_{xx} + \varepsilon_{yy} + \varepsilon_{zz}\right)\right),$$

$$\sigma_z = \frac{E}{1+\nu}\left(\varepsilon_{zz} + \frac{\nu}{1-2\nu}\left(\varepsilon_{xx} + \varepsilon_{yy} + \varepsilon_{zz}\right)\right),$$

$$\tau_{xy} = 2G\varepsilon_{xy},$$

$$\tau_{yz} = 2G\varepsilon_{yz},$$

$$\tau_{xz} = 2G\varepsilon_{xz}. \tag{7}$$

In stress damage analysis, two characteristic times are typically used to describe the thermal interaction between CW laser radiation and laser optical components. These are the time for the radial heat flux to propagate from the irradiation region to the end of the component, and the time for the component to reach a steady-state condition[42]. The temperature–time curve is shown in Figure S4 (Supplementary Material). The results indicate that the temperature reached equilibrium at approximately 20 s, which contributed to determining the possible time for the occurrence of damage. We considered only the thermal interaction within the second characteristic time of radiation. The damage mechanism can be elucidated by studying the internal temperature and stress of the crystal at thermal equilibrium.

Figure 4 shows the temperature gradient in the x-direction of the crystal surface for different pump powers. When the pump power was increased from 4.17 to 16.50 W, the maximum temperature gradient on the pumped surface of the 1% Er:CaF$_2$ crystal occurred near the edge of the spot, with peaks from –18 to –73 K/mm, whereas the peak temperature gradient on the pumped surface of the 2% Er:CaF$_2$ crystal occurred at the same location. However, the temperature gradient at the surface was much larger, with peaks ranging from –38 to –144 K/mm. We observed that the temperature

gradient increased with increasing pump power. The temperature gradient is a direct cause of thermal stress, and its increase indicated a continuous increase in the stress level. The temperature along the x-axis is shown in Figure S5 (Supplementary Material).

The stresses generated by the temperature gradients are referred to as thermal stresses. Strictly, thermal stress problems are coupled problems in which the temperature and deformation mutually influence each other. When analyzing one field, the effect of the other is treated as an external load.

The damage morphology of the crystals shows regular cracks with obvious orientation. Therefore, it is the stress in the direction of the crack that is of interest. Whether the crystal is damaged or not is determined by comparing the stress in a particular direction with the tensile and compressive strength of the material. The circumferential stress field at $x = 0$ in the yz cross-section of the crystal at the LIDT for two different doping concentrations was determined using finite-element calculations. Figure 5(b) shows the thermal stress field of the 1% Er:CaF$_2$ crystal at a power density of 192.5 kW/cm^2 (pump power density when damage occurs in 1% Er:CaF$_2$) for a pump power of 38.71 W. The maximum tensile stresses occurred at $x = z = 0$ and $y = 0.08$, resulting in $\sigma_{xx} = 34.54$ MPa. The maximum compressive stress in the crystal was –45.95 MPa. Similarly, Figure 5(c) shows the thermal stress field in the 2% Er:CaF$_2$ crystal for a pump power of 20 W corresponding to a power density of 99.8 kW/cm^2 (pump power density when damage occurs in 2% Er:CaF$_2$). In this case, the maximum tensile stress occurred in the crystal at $x = z = 0$, $y = 0.08$, resulting in $\sigma_{xx} = 34.38$ MPa, and the maximum compressive stress inside the crystal was –45.83 MPa.

The tensile strength was significantly lower than the compressive strength of the brittle materials[43,44]. According to previous studies, the tensile strength[45] and compressive strength of CaF$_2$ are 34 and 300 MPa, respectively. Therefore, the location of the maximum tensile stress is considered a potential starting point for mechanical damage.
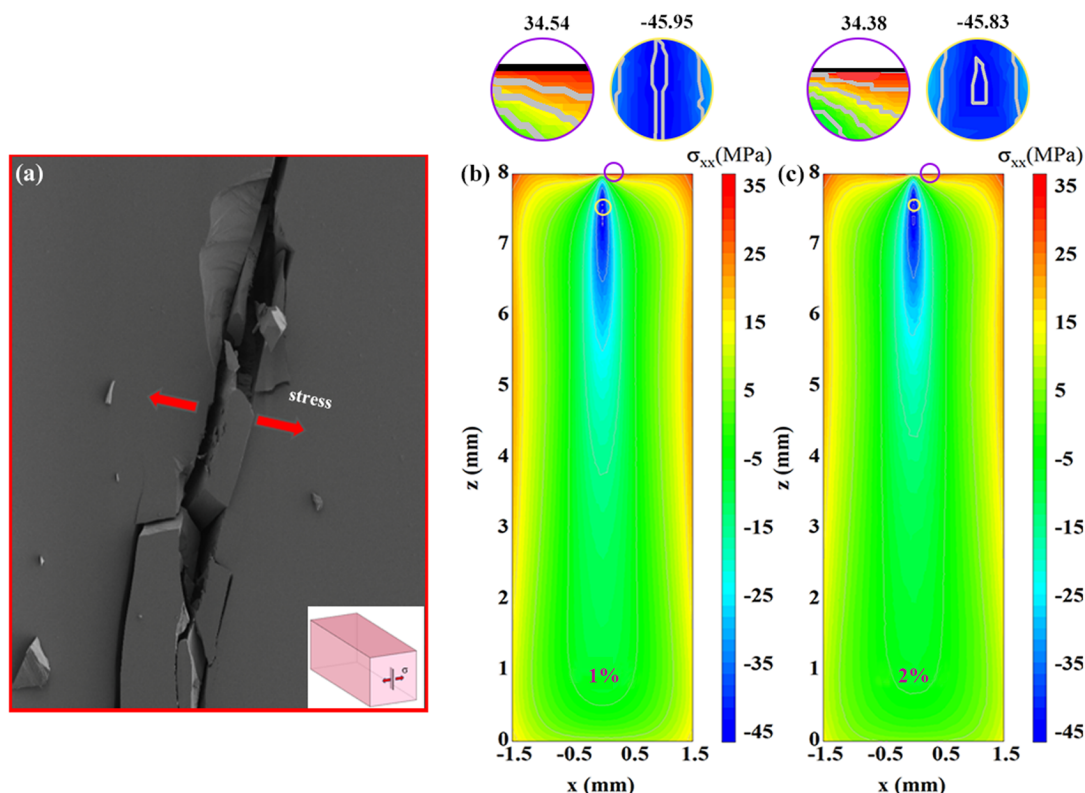
Figure 5. (a) Schematic of crystal fracturing under tensile stress. Stress fields of (b) 1% Er:CaF$_2$ and (c) 2% Er:CaF$_2$ crystals as damage occurs, calculated with a three-dimensional finite-element coupled thermodynamic model.

When the maximum tensile stress (1% Er:CaF$_2$, 34.54 MPa; 2% Er:CaF$_2$, 34.38 MPa) reaches the tensile strength 34.00 MPa, the maximum compressive stress (1% Er:CaF$_2$, –45.95 MPa; 2% Er:CaF$_2$, –45.83 MPa) is significantly lower than the compressive strength (–300.00 MPa). These findings suggest that laser-induced damage in Er:CaF$_2$ is caused by tensile stress and occurs at the edge of the beam spot on the pumping end surface.

Furthermore, crystals with higher doping concentrations exhibit lower LIDTs, primarily because of their stronger pump light absorption. At the same pump power, the crystals with higher doping concentrations experience larger temperature gradients, resulting in higher internal stresses. Consequently, they are more susceptible to damage under high-power laser irradiation. In contrast, doping can also alter the thermal conductivity characteristics of a crystal. Higher doping concentrations typically result in reduced thermal conductivity in the crystal, because doping impurities may introduce lattice defects or scattering centers, thereby attenuating the conduction of thermal energy[46]. This results in higher crystal temperatures under laser irradiation and increases the risk of damage.

The results of this study provide a foundation for the crystal parameter selection, thermal compensation and cavity design of 976 nm end-pumped Er:CaF$_2$ lasers. The influence of the crystal doping concentration on the LIDT and the role of internal stress during damage occurrence were clarified through experimentation and calculations. Theoretically, the LIDT can be enhanced by controlling the crystal concentration and designing thermal compensation structures to minimize the temperature gradient and stress within the crystal. For example, the use of gradient-doped crystals enables effective thermal management by minimizing temperature gradients during laser irradiation. In addition, a combination of materials with different thermal expansion can be used to compensate for or equalize the dimensional changes caused by temperature changes, thus reducing thermal stresses. By analyzing the temperature and stress fields in the crystal under laser irradiation, it is feasible to determine the laser damage mechanism of the material and evaluate the laser damage resistance of the crystal, and this kind of idea can also be used to analyze the damage mechanism of other gain crystals.

5. Conclusion

In this study, the damage mechanism of Er:CaF$_2$ crystals pumped by a 976 nm CW laser end face was investigated. The LIDTs of the crystals were 192.5 and 99.8 kW/cm^2 for 1% and 2% Er:CaF$_2$, respectively. The temperature and stress fields in the crystal were obtained through numerical calculation. Importantly, even when the pump power reached the LIDT, the maximum temperature (1% Er:CaF$_2$, 182°C;

2% Er:CaF$_2$, 218°C) at the surface remained significantly below the melting point (1362°C), suggesting that the damage mechanism is independent of melting. The presence of 70° regular cracks in the damage morphology suggests that the damage is stress-related and initiated in a specific crystallographic direction (slip system). Finite-element calculations indicated that the maximum tensile stress (1% Er:CaF$_2$, 34.54 MPa; 2% Er:CaF$_2$, 34.38 MPa) in the crystal at the time of damage reached the tensile strength of the crystal 34.00 MPa. This explains why the damage occurs before the melting point of the crystal is reached. At the same irradiation power, the crystals with a low doping concentration have a lower center temperature and stress, making them less susceptible to damage. In future research, the output power of MIR solid-state lasers will be further improved using sliced crystals to increase the heat dissipation area and a gradient doping process to eliminate the temperature gradient.

Acknowledgements

Supplementary material

The supplementary material for this article can be found at https://doi.org/10.1017/hpl.2024.44.

References

1. C. R. Petersen, U. Moller, I. Kubat, B. B. Zhou, S. Dupont, J. Ramsay, T. Benson, S. Sujecki, N. Abdel-Moneim, Z. Q. Tang, D. Furniss, A. Seddon, and O. Bang, Nat. Photonics **8**, 830 (2014).
2. M. Wang, Y. Wang, Y. Wu, H. Ma, H. Jiang, Y. Zhao, Y. Peng, W. Li, Y. Leng, K. M. Yu, and J. Shao, Adv. Funct. Mater. **34**, 2307234 (2023).
3. G.-W. Truong, L. W. Perner, D. M. Bailey, G. Winkler, S. B. Cataño-López, V. J. Wittwer, T. Südmeyer, C. Nguyen, D. Follman, A. J. Fleisher, O. H. Heckl, and G. D. Cole, Nat. Commun. **14**, 7846 (2023).
4. J. Shi, T. T. W. Wong, Y. He, L. Li, R. Zhang, C. S. Yung, J. Hwang, K. Maslov, and L. V. Wang, Nat. Photonics **13**, 609 (2019).
5. J. Kasparian, M. Rodriguez, G. Méjean, J. Yu, E. Salmon, H. Wille, R. Bourayou, S. Frey, Y.-B. André, A. Mysyrowicz, R. Sauerbrey, J.-P. Wolf, and L. Wöste, Science **301**, 61 (2003).
6. L. Yu, J. Liang, Q. Zeng, J. Wang, X. Luo, J. Wang, P. Yan, F. Dong, X. Liu, Q. Lü, C. Guo, and S. Ruan, High Power Laser Sci. Eng. **11**, e53 (2023).
7. Y. O. Aydın, V. Fortin, F. Maes, F. Jobin, S. D. Jackson, R. Vallée, and M. Bernier, Optica **4**, 235 (2017).
8. G. Brasse, R. Soulard, J. L. Doualan, A. Braud, A. Benayad, and P. Camy, J. Luminescence **232**, 1068329 (2021).
9. X. Duan, L. Li, X. Guo, Y. Ding, B. Yao, L. Zheng, L. Su, and Y. Wang, Opt. Express **26**, 26916 (2018).
10. D. K. Sardar and L. B. Levy, J. Appl. Phys. **79**, 1759 (1996).
11. J. Ma, Z. P. Qin, G. Q. Xie, L. J. Qian, and D. Y. Tang, Appl. Phys. Rev. **6**, 29 (2019).
12. J. Liu, J. Liu, J. Yang, W. Ma, Q. Wu, and L. Su, Opt. Lett. **42**, 3908 (2017).
13. D. A. Li, G. B. Zhang, J. Zhao, Y. T. Hu, Y. Lu, H. Zhang, Q. N. Li, D. Z. Zhang, R. Sha, F. Q. Shao, Z. M. Sheng, and T. P. Yu, High Power Laser Sci. Eng. **11**, e9 (2023).
14. E. V. Zharikov, V. Zhekov, L. A. Kulevskiĭ, T. M. Murina, V. V. Osiko, A. M. Prokhorov, A. D. Savel'ev, V. V. Smirnov, B. P. Starikov, and M. I. Timoshechkin, Sov. J. Quantum Electron. **4**, 1039 (1975).
15. R. C. Stoneman and L. Esterowitz, Opt. Lett. **17**, 816 (1992).
16. Z. Qin, G. Xie, H. Gu, T. Hai, P. Yuan, J. Ma, and L. Qian, Adv. Photonics **1**, 065001 (2019).
17. J. Chen, D. Sun, J. Luo, H. Zhang, R. Dou, J. Xiao, Q. Zhang, and S. Yin, Opt. Express **21**, 23425 (2013).
18. R. S. Quimby and W. J. Miniscalco, Appl. Opt. **281**, 14 (1989).
19. Y. Wang, F. Ma, Z. Zhang, Y. Wang, Q. Wu, J. Liu, J. Liu, Z. Chen, and L. Su, J. Luminescence **252**, 119339 (2022).
20. J. Liu, X. Feng, X. Fan, Z. Zhang, B. Zhang, J. Liu, and L. Su, Opt. Lett. **43**, 2418 (2018).
21. Z. Yang, Z. Zhang, Z. Zhao, L. Su, and Z. Liu, Chinese J. Lasers **51**, 1701006 (2024).
22. C. T. Wu, M. X. Yao, T. Y. Dai, and Y. L. Ju, Optik **140**, 356 (2017).
23. L. Cini and J. I. Mackenzie, Appl. Phys. B **123**, 273 (2017).
24. J. Liu, X. Chen, Y. Yu, C. Wu, F. Bai, and G. Jin, Phys. Rev. A **93**, 013854 (2016).
25. H. Johansen, S. Gogoll, E. Stenzel, M. Reichling, and E. Matthias, Radiat. Effects Defects Solids **136**, 151 (1995).
26. M. Azumi, G. J. Exarhos, E. Nakahata, V. E. Gruzdev, J. A. Menapace, D. Ristau, and M. J. Soileau, Proc. SPIE **7842**, 78421U (2010).
27. G. J. Exarhos, V. E. Gruzdev, J. A. Menapace, D. Ristau, M. J. Soileau, M. Azumi, and E. Nakahata, Proc. SPIE **9632**, 963213 (2015).
28. J. Shao, X. Liang, Y. Lin, S. Wang, Z. Deng, G. Meng, and X. Fang, Appl. Surface Sci. **586**, 152716 (2022).
29. P. Balling and J. Schou, Rep. Prog. Phys. **76**, 036502 (2013).
30. I. Pipinytė, V. Tamulienė, J. Vengelis, M. Sirutavičius, R. Grigonis, and V. Sirutkaitis, Opt. Eng. **59**, 016102 (2020).
31. A. E. Chmel, Mater. Sci. Eng. B **49**, 175 (1997).
32. Z. K. Lou, K. Han, C. F. Zhang, M. S. Chen, B. Z. Yan, Y. Yang, H. Liu, J. Chen, and X. Li, Phys. Scr. **95**, 035507 (2020).
33. J. H. Zhao, X. Y. Li, H. Liu, R. Q. Jiang, Z. P. Liu, Z. H. Hu, H. M. Gong, and J. X. Fang, Appl. Phys. Lett. **74**, 1081 (1999).
34. Z. H. Zhou, W. Liu, H. Z. Yan, X. F. Chen, and W. J. Wan, Adv. Photonics **4**, 045001 (2022).
35. S. U. Liangbi, W. U. Qinghui, F. Wei, K. O. U. Huamin, L. I. Xiang, and W. Xu, J. Inorganic Mater. **747**, 359 (2024).
36. M. Zong, X. Yang, J. Liu, Z. Zhang, S. Jiang, J. Liu, and L. Su, J. Luminescence **227**, 117519 (2020).
37. P. Zhang, W. Liao, Z. Zhu, M. Qin, Z. Zhang, D. Jin, Y. Liu, Z. Wang, Z. Lu, and R. Xiong, Phys. Chem. Chem. Phys. **25**, 15422 (2023).
38. Z. D. Liu, B. C. Mei, J. H. Song, and W. W. Li, J. Am. Ceramic Soc. **97**, 2506 (2014).

39. A. V. Kuanr, S. K. Bansal, and G. P. Srivastava, Opt. Laser Technol. **28**, 25 (1996).
40. X. Wang, J. Z. Shao, H. Li, J. S. Nie, and X. D. Fang, Opt. Eng. **55**, 027102 (2016).
41. W. P. Mason, J. Acoust. Soc. Am. **28**, 1197 (2005).
42. A. A. Blistanov, N. M. Voloshinskaya, E. P. Glotov, K. Z. Gubaĭdullina, I. A. Zabolotskikh, V. N. Koterov, O. M. Kugaenko, V. V. Sumerin, V. A. Ul'yanov, N. V. Cheburkin, and Y. M. Shcherbakov, Sov. J. Quantum Electron. **14**, 1583 (1984).
43. G. Brambilla and D. N. Payne, Nano Lett. **9**, 831 (2009).
44. K. Zheng, C. Wang, Y.-Q. Cheng, Y. Yue, X. Han, Z. Zhang, Z. Shan, S. X. Mao, M. Ye, Y. Yin, and E. Ma, Nat. Commun. **1**, 24 (2010).
45. M. J. Weber, *Handbook of Optical Materials* (CRC Press, Boca Raton, 2002).
46. Y. Dai, J. Dong, Z. Zhang, Z. Zhang, H. Kou, L. Su, J. Liu, J. Gao, R. Dou, Q. Zhang, and A. Wu, Crystal Growth Design **23**, 2343 (2023).